#### RESEARCH



# Study of Global Photospheric and Chromospheric Flows Using Local Correlation Tracking and Machine Learning Methods I: Methodology and Uncertainty Estimates

Qin Li<sup>1</sup> · Yan Xu<sup>1,2</sup> · Meetu Verma<sup>3</sup> · Carsten Denker<sup>3</sup> · Junwei Zhao<sup>4</sup> · Haimin Wang<sup>1,2</sup>

Received: 6 January 2023 / Accepted: 18 April 2023 © The Author(s) 2023

#### Abstract

Cyclical variations of the solar magnetic fields, and hence the level of solar activity, are among the top interests of space weather research. Surface flows in global-scale, in particular differential rotation and meridional flows, play important roles in the solar dynamo that describes the origin and variation of solar magnetic fields. In principle, differential rotation is the fundamental cause of dipole field formation and emergence, and meridional flows are the surface component of a longitudinal circulation that brings decayed field from low latitudes to polar regions. Such flows are key inputs and constraints of observational and modeling studies of solar cycles. Here, we present two methods, local correlation tracking (LCT) and machine learning-based self-supervised optical flow methods, to measure differential rotation and meridional flows from full-disk magnetograms that probe the photosphere and  $H\alpha$  images that probe the chromosphere, respectively. LCT is robust in deriving photospheric flows using magnetograms. However, we found that it failed to trace flows using time-sequence H $\alpha$  data because of the strong dynamics of traceable features. The optical flow methods handle  $H\alpha$  data better to measure the chromospheric flow fields. We found that the differential rotation from photospheric and chromospheric measurements shows a strong correlation with a maximum of 2.85 µrad s<sup>-1</sup> at the equator and the accuracy holds until 60° for the MDI and  $H\alpha$ , 75° for the HMI dataset. On the other hand, the meridional flow deduced from the chromospheric measurement shows a similar trend as the concurrent photospheric measurement within 60° with a maximum of 20 m s<sup>-1</sup> at 40° in latitude. Furthermore, the measurement uncertainties are discussed.

**Keywords** Sun: solar cycle · Sun: differential rotation · Sun: meridional circulation

☑ Q. Li ql47@njit.edu

Published online: 16 May 2023

<sup>&</sup>lt;sup>4</sup> W. W. Hansen Experimental Physics Laboratory, Stanford University, Stanford, USA



Space Weather Research Laboratory, New Jersey Institute of Technology, University Heights, Newark, NJ 07102-1982, USA

Big Bear Solar Observatory, New Jersey Institute of Technology, Big Bear City, CA 92314-9672, USA

<sup>&</sup>lt;sup>3</sup> Leibniz-Institut für Astrophysik Potsdam (AIP), Potsdam, Germany

**62** Page 2 of 16 Q. Li et al.

#### 1. Introduction

Differential rotation and meridional flow are global-scale flows that are among the most important manifestations of the solar dynamo (Parker, 1955; Steenbeck, Krause, and Rädler, 1966), and they contribute to solar cycle variations (Jørgensen et al., 2019). From the modeling perspectives, these flows provide essential inputs. For instance, in simulations of surface flux transport (Sheeley, 2005), the transport of the magnetic field at the solar surface undergoes a random walk process because of the supergranular flow, which is affected by differential rotation and meridional circulation.

Differential rotation describes the different angular speeds as a function of latitude on the solar surface (Schroeter, 1985). On top of the long-term average, differential rotation exhibits a zonal flow, where the temporal variation is known as torsional oscillation (Howard and Labonte, 1980; Zhao and Kosovichev, 2004; Howe, 2009; Howe et al., 2018). The meridional flow is an axisymmetric flow, in both polar and equatorial directions of motion (Hathaway and Upton, 2014b; Komm, Howe, and Hill, 2018). Meridional circulation is composed of a poleward meridional flow at the solar surface and an equatorward flow at the base of the convection zone, and appears to be single cell or multiple cells in solar cycles (Zhao et al., 2013; Gizon et al., 2020).

There are three common methods to measure global-scale solar surface flows: direct measurements of the Doppler or line-of-sight velocity (Hathaway et al., 1996; Ulrich, 2010), helioseismology techniques, (Basu, Antia, and Tripathy, 1999) and tracing moving features. In addition, other types of methods exist for measuring small-scale flows, i.e., minimum energy fit (Longcope, 2004) to study flows inside ARs, and supervised learning methods for flows in granulation (Asensio Ramos, Requerey, and Vitas, 2017). While Doppler measurement and helioseismology techniques measure line-of-sight components of the velocity field, tracing moving features, i.e., sunspots, and other magnetic features, infer the transverse component. Some methods infer both components of the velocity field (e.g., Longcope, 2004). Feature tracking of large-scale flows, including small magnetic features (Komm, Howard, and Harvey, 1993), sunspots (Howard and Gilman, 1986), and granulation (Rieutord et al., 2001) is not only limited to magnetograms and intensitygrams, but can be applied to different features in different atmospheric layers, small-scale bright coronal structure (i.e., Brajša et al., 2001; Wöhl et al., 2010) and radio features at 17 GHz (Chandra, Vats, and Iyer, 2009). The surface flow results may vary due to systematic errors, different methods, the height dependence of representative features, as well as the type of flows, such as physical flows and optical flows.

In general, the differential rotation and meridional flow profiles are key parameters to flux transport models used to predict the amplitude of solar cycles. Constant flows are often used in the flux transport model. While the differential rotation changes slightly, the variation of meridional flow is found to be more significant over the solar cycles or from cycle to cycle (i.e., Hathaway and Upton, 2014a). Therefore, observed time-varying differential rotation and meridional flow profiles are necessary for reproducing the realistic magnetic evolution. Archived data covering a long period, such as ten or more solar cycles, provide crucial information in understanding the solar dynamo and future solar cycles. The level of solar activity from about 1930 to 2020 was exceptionally high compared to other periods in the past 10,000 years (Solanki et al., 2004). Therefore, investigations of the past few cycles are especially beneficial in understanding this high level of activity, and some physical parameters found from these cycles can also be applied to assess upcoming cycles. It is well recognized by the solar physics community that Solar Cycle 23 is prolonged and Solar Cycle 24 is weaker compared to previous cycles. The most notable difference is the lack of



sunspots, i.e., the number of spotless days in both 2008 and 2009 was the highest in a century (Li, 2009). Consequently, the solar wind energy reached a record low, which may have significant impact on the influx of cosmic rays to Earth (Fisk and Zhao, 2009). What caused such unusual behaviors is of great interest. Furthermore, it is important to know if this trend continues for the transition from Cycle 24 to 25. Thus, long-term observations of previous solar cycles and well-designed studies will shed new light on solar cycle variation. However, consistent synoptic data suitable for flow tracking starts only in 1996, after the launch of the Solar and Heliospheric Observatory (SoHO, Domingo, Fleck, and Poland, 1995) and continues after the launch of the Solar Dynamics Observatory (SDO, Pesnell, Thompson, and Chamberlin, 2012). We target these 25 years to establish the feasibility of tracing flows using some less uniform datasets, which are available before 1996.

Among the available archives, the full-disk H $\alpha$  database, for instance, from the Global Hα Network (GHN) and the Kodaikanal Solar Observatory of the Indian Institute of Astrophysics, covers over 100 years and provides unique information of cycle variations, e.g., of filaments and prominences (i.e., Hao et al., 2015; Chatterjee et al., 2020; Tlatova, Vasil'eva, and Tlatov, 2020; Xu et al., 2021). On the other hand, extracting global-scale flows from the chromospheric data is difficult because of numerous small-scale flows in the low- $\beta$  plasma environment. In this study, we present two methods to derive optical flows, namely local correlation tracking (LCT, November and Simon, 1988) and machine learning-based selfsupervised optical flow methods, to derive the global-scale surface flows from  $H\alpha$  images, namely optical flows. The optical flows are then compared with the flows from helioseismology. The purpose of computing optical flows from magnetograms is to assess the capability of optical flow methods as an appropriate approximation of helioseismic measurements of differential rotation and meridional flows. Please note that optical flow is defined as the apparent motions on the image plane. Under certain conditions of spatial and temporal scales, optical flows can correlate very well with physical flows. Full-disk magnetograms from the Helioseismic and Magnetic Imager (HMI; Scherrer et al., 2012) on board SDO, the Michelson Doppler Imager (MDI; Scherrer et al., 1995), and full-disk H $\alpha$  maps from the Kanzelhöhe Solar Observatory (KSO, Pötzi et al., 2016, one of the GHN backbone stations) are used. LCT is a sophisticated method and has been widely used in constructing velocity fields. Since LCT performance is degraded for nonuniform motions present ubiquitously in the chromospheric data, the machine learning-based optical flow method is implemented on  $H\alpha$  images.

# 2. Data Processing and Methodology

#### 2.1. Data and Observations

The datasets include line-of-sight (LOS) magnetograms from SDO/HMI and SOHO/MDI, and H $\alpha$  line-core images from KSO. The data structure used in this study can be found in Table 1. HMI LOS magnetograms are limited to 15 images per day from 19:00 to 22:00 UT, with a cadence of 720 s, from 2010-06-15 to 2020-09-29. MDI LOS magnetograms are calculated for 15 images per day, with a cadence of 96 min, from 2000-01-15 to 2010-12-27. Similar to the phenomenon of granule tracking exhibiting a shrinking effect (Löptien et al., 2016), the center-to-limb variation is compromising the accuracy of feature tracking measurements (Imada and Fujiyama, 2018). Therefore, the HMI and MDI data undergo the center-to-limb correction procedure (Mahajan et al., 2021) that decomposes the measured velocity into three components: a systematic shift, a linear variation with time lag, and the



**62** Page 4 of 16 Q. Li et al.

Table 1	Summary	of HMI,	MDI, a	nd Hα	data.
---------	---------	---------	--------	-------	-------

Instrument	Time period	Cadence	Images per day	Resolution
MDI	2000-01-15 to 2010-12-27	96 min	~ 15	$\sim$ 2 arcsec
HMI	2010-06-15 to 2020-09-29	12 min	$\sim 15$	$\sim$ 0.5 arcsec
Ηα	2005-07-09 to 2010-04-16	$\sim 2 \text{ min}$	$\sim 100$	$\sim$ 0.5 arcsec

baseline velocity. By combining the measurements of displacements in three distinct time lags, the baseline velocity can be obtained. KSO H $\alpha$  full-disk images are selected between 07:00 UT and 15:00 UT from 1998-09-24 to 2021-04-05, and then segmented to 100 2-minute cadence images. In this study, H $\alpha$  images are investigated, which overlap with MDI datasets from 2005-07-09 to 2010-04-16. In addition to standard dark and flat field corrections, limb-darkening removal, P-angle correction, and de-stretching are carried out to obtain a consistent time-series of H $\alpha$  images. Furthermore, Zernike polynomials and a high-pass filter are applied to remove transmission artifacts of narrow-band filters (Shen, Diercke, and Denker, 2018). To reduce noise and avoid projection effects, polar regions beyond  $\pm 75^{\circ}$  in longitude are excluded for both magnetograms and H $\alpha$  images. Helioseismic measurements are obtained from the time-distance helioseismology data-analysis pipeline that was implemented at the HMI-AIA Joint Science Operation Center, and preprocessed by Zhao et al. (2012).

## 2.2. Local Correlation Tracking

LCT calculates the displacement vectors of two small regions in consecutive images by maximizing the cross-correlation coefficient, and we use the implementation of Verma and Denker (2011) in this study. This is a well-developed method, often used in studying photospheric and chromospheric horizontal flows. An example and detailed introduction can be found in Verma and Denker (2012). The LCT algorithm necessitates the assumption of constant velocity, which is inconsistent with the magnetic induction equation (Schuck, 2005). This limitation of LCT renders it less effective than NAVE and DAVE (Chae and Sakurai, 2008) in detecting nonuniform motions. In the application of LCT to full-disk image series, the motion involves superpixels and a combination of nonuniform local flows and uniform global-scale flows. By averaging over a low-cadence and large-size window, local flows are suppressed, highlighting the uniform flows. However, LCT may underestimate the actual velocities at the surface (Verma, Steffen, and Denker, 2013). Despite this drawback, LCT remains highly time-efficient.

In bulk-processing time-series data of HMI, MDI, and H $\alpha$  images, the cadence, kernel size, and FWHM of the Gaussian sampling window are carefully chosen. The kernel size is set to cover the maximum pixel shift at the equator. FWHM is roughly the size of the tracking features or granulation to super granulation from a few thousand to tens of thousands of kilometers in deriving global-scale flows. Sampling window and kernel size of  $16 \times 16$  pixels with a FWHM = 3600 km are applied for processing HMI LOS magnetograms. MDI data has a much higher cadence that ends up using a larger kernel size of  $44 \times 44$  pixels with a FWHM = 20400 km. KSO H $\alpha$  images use a kernel size of  $12 \times 12$  pixels and FWHM = 4800 km. When utilizing large sampling windows and longer time lags to ascertain the photospheric flows, we are predisposed towards tracking stronger magnetic features. This may cause some biases, e.g., sunspots may rotate slightly faster than surrounding quiet Sun, or stronger magnetic elements exhibiting faster rotation and meridional circulation



speeds (Imada and Fujiyama, 2018). These differences give uncertainty caused by the bias. A systematic benchmarking of LCT performance on simulated continuum images can be found in Verma, Steffen, and Denker (2013). After using LCT to calculate the velocity field, the apparent velocity  $v_x$  and  $v_y$  from the reference frame in helio-projective Cartesian coordinates is converted to de-projected  $v_{\phi}$  and  $v_{\theta}$  in spherical coordinates, considering the finite distance from the center of the Sun to the observer (Löptien et al., 2017). Then, the flow maps are converted to heliographic coordinates and in a grid from S75° to N75° with an increment of 1°. The transformation from  $v_x$  and  $v_y$  to  $v_{\phi}$  and  $v_{\theta}$  assumes that the movements are purely horizontal at the surface with  $V_r = 0$ . While the resulting potential error from this assumption may be minimal at the disk center, it may reach up to  $\sim 1 \text{ km s}^{-1}$  at the limb, which can be mitigated by averaging over both the east and west sides. In determining chromospheric flows, however, the upward motions from the background (e.g., spicules and jets) may not be negligible. Nevertheless, these motions are short-lived, and when averaged over an extended period and both sides of the solar disk, their effect should be minimized.

# 2.3. Self-Supervised Optical Flow Method

LCT has been used to study optical flows from high-resolution images collected by ground-based and space-based observatories, yet, it has the drawback of deriving continuous flows from nonuniform or nonrigid motions. Computer vision researchers have developed an alternative method to derive optical flows from relative motions of objects in digital images (Hurlburt and Jaffey, 2015), which is named *Optical Flow*. *Optical Flow* assumes that the local intensity is advected by the velocity field of each pixel. Generally, images are taken at a cadence where the displacement is smaller than one pixel. Therefore, the challenge and limitation of *Optical Flow* includes large-scale displacements, strong intensity gradient, and occlusion. The latter is defined as when specific pixels disappear in the subsequent images (Hur and Roth, 2020). One of the differences between a typical machine vision problem and deriving fluid velocities is that the former calculates the motion of a discrete object while the latter seeks the motions of a continuous flow. In the process of deriving the continuous flows, real velocities can be underestimated due to the chosen sampling windows, which is also related to the lifetime of tracking patterns, i.e., magnetic diffusion.

The traditional Optical Flow method is formulated as a minimization problem and is generally computationally expensive. Recently, deep learning has been widely used for image classification problems and has been deployed to solve other computer vision problems, such as tracking optical flows using Flownet (Dosovitskiy et al., 2015) or end-to-end deep learning to estimate simulated physical flows (Asensio Ramos, Requerey, and Vitas, 2017). The development of the optical flow learning method can be traced back to FlowNet (Mayer et al., 2015). Yet, the supervised optical flow method requires a large amount of densely labeled data. To get around this limitation, one solution is to use synthetic datasets. Yet, previous studies have shown a large domain gap between the distribution of synthetic images and real images. Here, we used the self-supervised optical flow method (DDflow, Liu et al., 2019) to derive the flow field in H $\alpha$  datasets, which generates annotations on unlabeled data using a model trained with Optical Flow, and then retrain the model using the generated annotations. The approach simultaneously trains two CNNs and distills reliable predictions from a teacher network and uses these predictions to guide a student network. Training is conducted from the challenging Flying Chairs, MPI Sintel, KITTI 2012 and 2015 benchmarks. This method is applied to the archived five-year  $H\alpha$  data using the pre-trained model and make a parallel comparison with MDI data using LCT in the same period.



**62** Page 6 of 16 Q. Li et al.

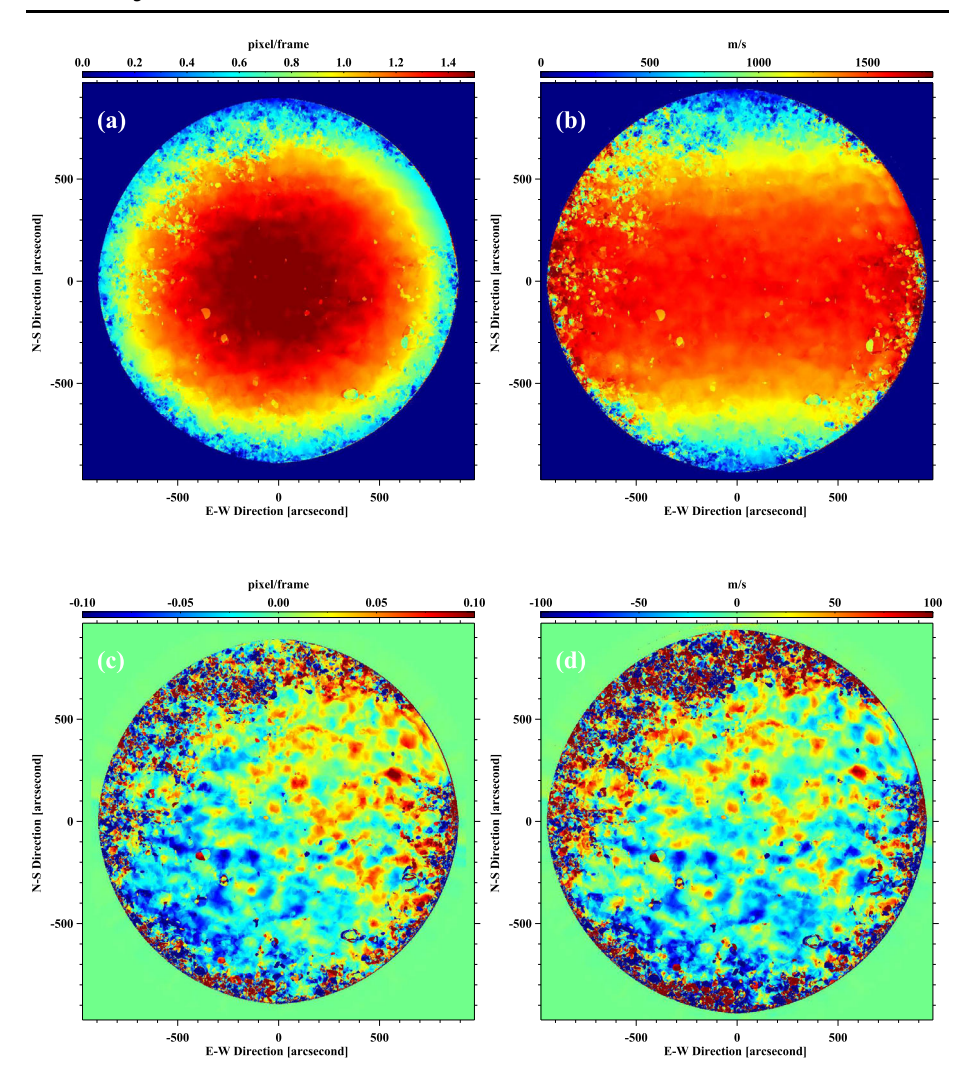


**Figure 1** Global-scale flow map derived by LCT from MDI LOS magnetogram on 2010-11-27. Left: original LCT flow map, right: remapped flow map. (a) Flow map for  $v_x$ . (b) Flow map for  $v_{\phi}$ . (c) Flow map for  $v_{\phi}$ . (d) Flow map for  $v_{\theta}$ .

## 3. Results

The fundamental elements of LCT calculations are image pairs containing two consecutive images or two images with a certain time delay. For MDI data, 24-hour time series is used. Figure 1 shows the results of the averaged photospheric flows of 15 image pairs on 2010-11-27.  $v_x$  ranges from 0.0 to 1.5 pixels frame<sup>-1</sup> while  $v_y$  ranges from -0.10 to 0.10 pixels frame<sup>-1</sup>. The choice of this velocity representation remains the same for other MDI observations. The introduced systematic error due to such velocity representation will be discussed later. LCT velocities are derived in the plane-of-sky, which peak at disk center and decrease towards the limb due to projection effects. Considering the finite distance to the observer, it is necessary to convert the plane-of-sky velocity in helio-projective Carte-



sian coordinates to the real velocity in heliographic coordinates with the projection effect removed. The right column of Figure 1 illustrates the remapped flow maps in the longitudinal and latitudinal direction. The velocity fields  $v_x$  and  $v_y$  in Cartesian coordinates are converted to  $v_\phi$  and  $v_\theta$  in heliographic coordinates by following the coordinate conversion procedure in Thompson (2006) and Löptien et al. (2017). Therefore,  $v_\phi$  and  $v_\theta$  are defined as differential rotation and meridional flow, respectively. The meridional flow is two to three orders of magnitude lower than the differential rotation. Active regions are invisible in the  $v_\phi$  map, but recognizable in the  $v_\theta$  map. Therefore, the presence of an active region has little impact in deriving the differential rotation compared to meridional flow. A smooth transition from the faster band at the equator to the slower band toward the poles is clearly present. A similar but more clear pattern can also be observed in HMI flow maps using the same LCT method on 2010-12-07 in Figure 2. After remapping, the cells of meridional flows in each hemisphere become more clear.

The derived transverse flows can vary because of differently chosen FWHM of the Gaussian sampling window, cadences, and the number of flow maps that are averaged (Verma and Denker, 2011). The exact FWHM, cadences, and elapsed time used in this study are given in Section 2.2. Elapsed time refers to the number of image pairs to be averaged in LCT or *Optical Flow*. As different scales of velocities are unavoidable, we apply a linear transformation upon all the measurements in terms of differential rotation deduced from helioseismology. Figure 3 shows an example of one-day differential rotation and meridional flow profiles on 2010-06-15 after linear transformation correction. The one-day flow maps from both HMI and MDI are derived from 15 daily image pairs. Differential rotation profiles from HMI and MDI magnetograms exhibit a moderate match below  $60^{\circ}$ . The meridional poleward flows peak at mid-latitude and start to decrease beyond  $50^{\circ}$ . The quality of the meridional flow profile from MDI may not be as good as that from HMI LOS magnetograms, yet, the meridional flow symmetry is still visible. The minor shifting of the meridional flow profile is due to the projection effect of the  $B_0$ -angle variation. This cancels out in long-term temporal profile or average profile.

Figure 4 shows the 10-year average profile of differential rotation and meridional flow from HMI and MDI LOS magnetograms, and helioseismology measurement. The error bars represent the standard deviation at different latitudes for the 10-year average flow maps. From the measurements, the rotation speed at the equator is 2.85 µrad s<sup>-1</sup> which is compatible with previous studies (Beck, 2000). As HMI has a higher spatial resolution, the rotation speed deduced from HMI keeps decreasing, and can reach as low as 1.1  $\mu$ rad s<sup>-1</sup> at the pole. MDI, however, stops following the trend after 60° due to the limitation of resolution and up to 30% magnetic sensitivity variation at the limb (Liu, Zhao, and Hoeksema, 2004), which becomes more significant beyond 70° when the feature patterns can hardly be recognized. A similar rapid changes of gradient in meridional flow can also be observed at  $\sim 60^{\circ}$  in MDI and  $\sim 75^{\circ}$  in HMI because the flows are overestimated. In Solar Cycles 23 and 24, the meridional flow peaks at about 50° latitude in the southern/northern hemisphere. Before the linear transformation, the different amplitudes of velocity peaks from HMI and LCT are the result of using different spatial resolutions and cadences. The meridional flows derived from LCT do not fall into the range of helioseismic analysis (Zhao et al., 2012) or the magnetic feature tracking results (Hathaway and Rightmire, 2010) of  $\pm 15 \,\mathrm{m\,s^{-1}}$  but close to the granulation tracking results of -25 to  $30 \text{ m s}^{-1}$ , which reflects the great impact from the moat flows around the sunspot region in meridional direction (Roudier et al., 2018). Compared to the previous two methods, our results reflect the tracking results from a combination of all features on the solar surface, i.e., quiet Sun, plage, sunspots. Besides, tracking magnetic features with lower than 100 G can affect the results of both differential rotation and meridional



**62** Page 8 of 16 Q. Li et al.

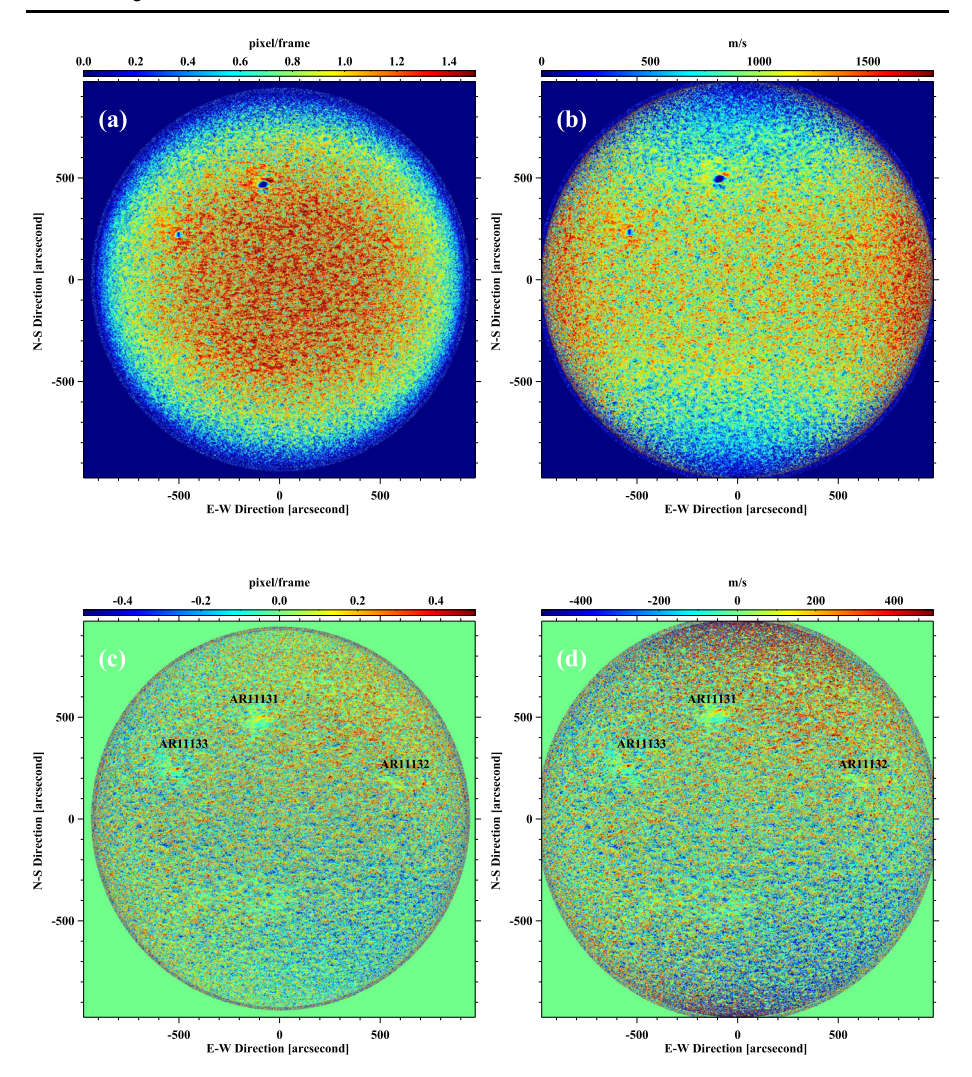


**Figure 2** Global-scale flow map derived by LCT from HMI LOS magnetograms on 2010-12-07. Left: original LCT flow map, right: remapped flow map. (a) Flow map for  $v_x$ . (b) Flow map for  $v_\phi$ . (c) Flow map for  $v_y$ . (d) Flow map for  $v_\theta$ .

circulation (Imada and Fujiyama, 2018). Furthermore, extending the cadence by a few more hours may also reduce the amplitude of flows. The peaks of the meridional flow derived from the pattern tracking method are always located at a higher latitude than those from either Doppler or helioseismic measurements (Dikpati, Gilman, and Ulrich, 2010). One reason is that the active region inflows may disturb the poleward meridional flows (Braun, 2019), the discrepancy between the meridional flows in active regions and quiet Sun can also be seen in Figure 1. Another reason is surface turbulent magnetic diffusion, which reduces the tracking speed at low latitudes but adds speed at high latitudes (Dikpati, Gilman, and Ulrich, 2010). The FWHM of the meridional flow in each hemisphere is also related to sunspot groups in the activity belt. The sunspots' presence may disturb the meridional flow's move-



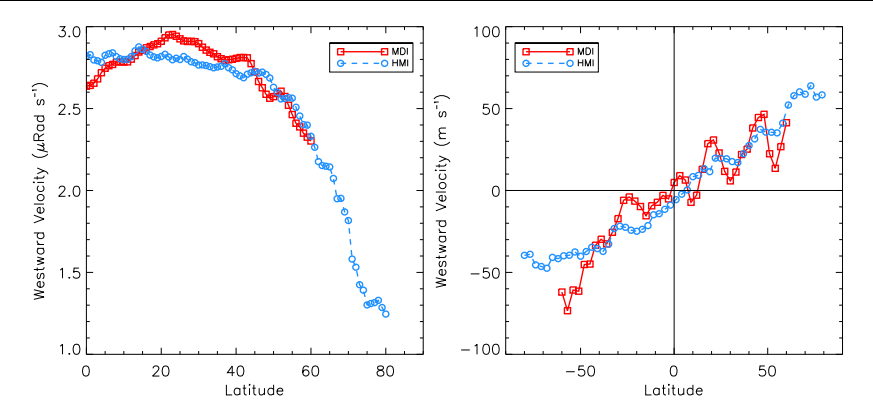


**Figure 3** One-day profiles of differential rotation (left) and meridional flows (right) obtained from HMI (blue) and MDI (red) LOS magnetograms on 2010-06-15.

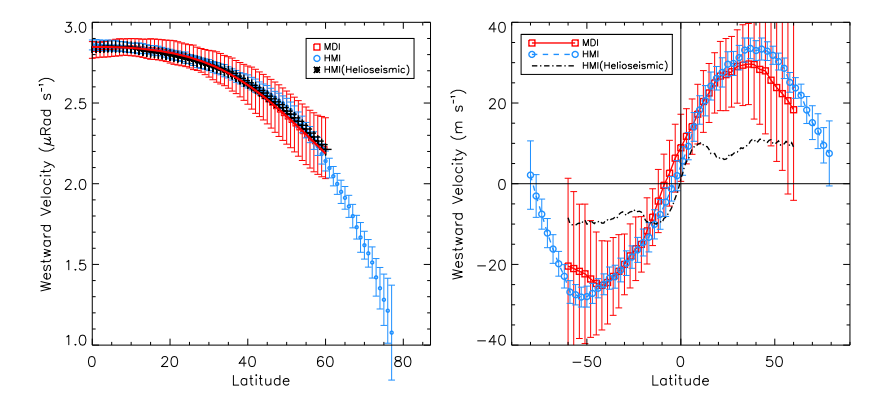


Figure 4 10-year average profiles of differential rotation (left) and meridional flows (right) obtained from HMI (blue, June 2010 to August 2020), MDI (red, January 2000 to December 2010) LOS magnetograms and helioseismology measurements (black, May 2010 to May 2021). Solid lines represent fits to each type of the data. In MDI measurements, the flows at  $60^{\circ}$  is ignored due to the limitation of spatial resolution/magnetic sensitivity at the limb.

ment, suggesting a weaker meridional flow accompanies a more robust cycle, which has an increasing number of sunspots. It also agrees with the interpretation of the Solar Cycle 23 (Zhao and Kosovichev, 2004) that an inflow toward the active latitudes superposed on a general poleward meridional flow weakens the meridional flow.

By using the self-supervised *Optical Flow* method, the derived one-day flow map from a four-hour sequence with 100 pairs of H $\alpha$  images is shown in Figure 5. Since the cadence and observational time are not constant for each day, we carry out the daily flow tracking only on days with at least four hours coverage and 100 pairs of images. The velocity field  $v_x$  and  $v_y$  have also been remapped to  $v_\phi$  and  $v_\theta$  in heliographic coordinates. There is a high uncertainty at high longitudes, but it is negligible as we only consider the range  $\pm 75^\circ$ . Please note that the flow speed in the north/south hemisphere is averaged in order to avoid the effect of the p-angle variation in the archived database. The differential rotation derived from H $\alpha$  images is similar but less accurate than that from MDI and HMI. The meridional circulation cells are discernable. However, due to the hemispheric averaging, the asymmetry



**62** Page 10 of 16 Q. Li et al.

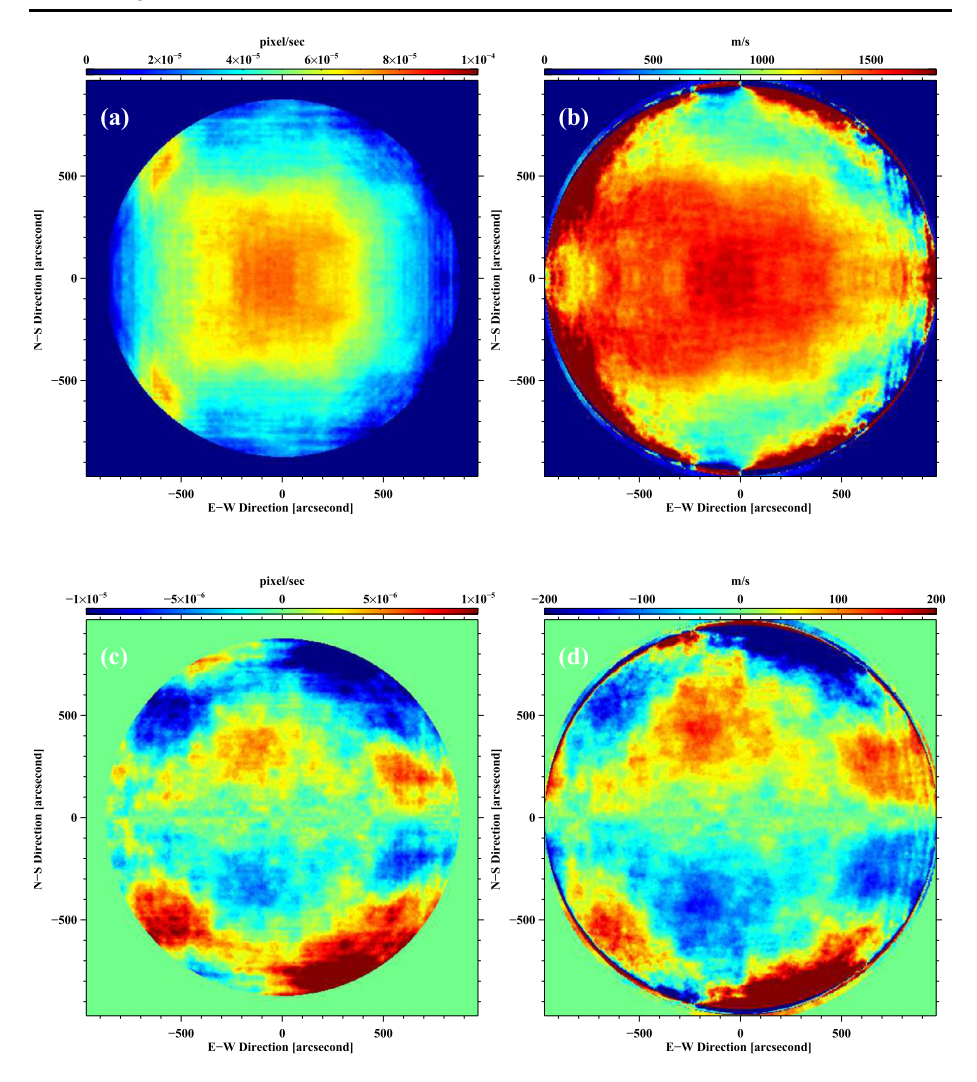


**Figure 5** Global-scale flow map derived by *Optical Flow* from HMI LOS magnetograms on 2010-12-07. Left: original LCT flow map, right: remapped flow map. (a) Flow map for  $v_x$ . (b) Flow map for  $v_\phi$ . (c) Flow map for  $v_\phi$ . (d) Flow map for  $v_\theta$ .

of the meridional circulation is undetermined. The comparison of the differential rotation and meridional flow profiles derived from MDI LOS magnetograms and KSO H $\alpha$  images using LCT and *Optical Flow* are shown in Figure 6. We choose the same time period from July 2005 to September 2010. We labeled KSO "OF" and KSO "LCT" to represent the data source and method that was used to derive the flow maps. The error bars represent the standard deviation at different latitudes for the 5-year average flow maps. Both *Optical Flow* and LCT methods can produce similar differential rotation profiles below 45° which begins as 2.85  $\mu$ rad s<sup>-1</sup> at the equator and keep decreasing. However, only *Optical Flow* can trace the differential rotation down to 2.30  $\mu$ rad s<sup>-1</sup> at 60° and above. A turning point at about 60° also applies to KSO data as a result of lower resolution and noise, and it also becomes



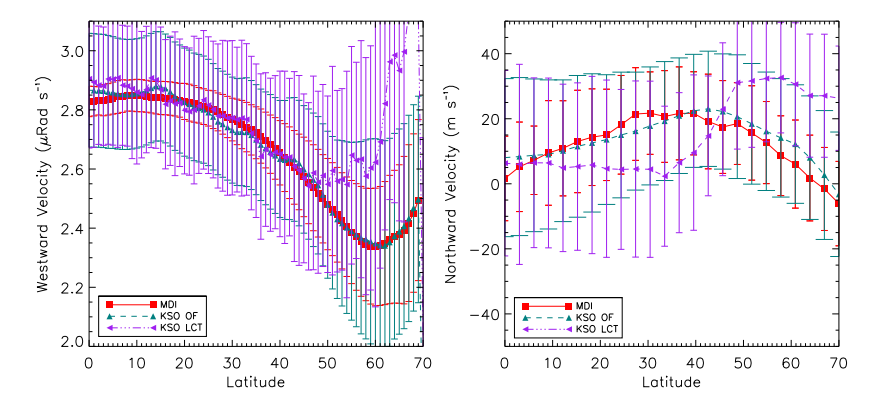


**Figure 6** Left: Average profile of differential rotation obtained from MDI LOS magnetograms (red) and KSO Hα images using *Optical Flow* (blue) and LCT (purple) methods, in the time period from July 2005 to September 2010. Right: Average profile of meridional flows obtained from MDI LOS magnetograms (red) and KSO Hα images using *Optical Flow* (blue) and LCT (purple) methods, in the time period from July 2005 to September 2010. In both Hα and MDI measurements, the turning point at about  $60^{\circ}$  is a result of spatial resolution/magnetic sensitivity at the limb.

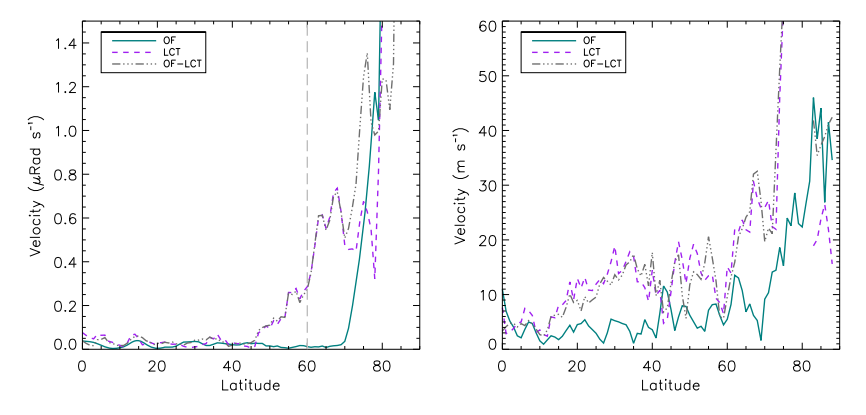


**Figure 7** The difference between *Optical Flow* and LCT with MDI flow profiles using LCT for the differential rotation profile (left) and the meridional rotation profile (right).

more significant beyond 70°. The differential rotation profiles from MDI and KSO *Optical Flow* show a stronger correlation that with KSO LCT, with 16.1% and 15.6% relative error, respectively. KSO LCT produces similar result of differential rotation velocity only up to 50°, with 11.6% relative error. Overall, the meridional flow profiles from MDI and KSO *Optical Flow* show a consensus trend and similar up-and-down pattern within 70°. The meridional flow from MDI reaches the maximum of 20 m s<sup>-1</sup> at 30° while that from *Optical Flow* reaches the maximum of 20 m s<sup>-1</sup> at 40°. KSO LCT, however, fails to derive reasonable flow patterns by not showing a clear peak value with latitudes. The difference between KSO LCT and MDI can reach 20 m s<sup>-1</sup> below 45°. Besides the systematic error source, the uncertainty is also affected by the  $B_0$ -angle variation, which has more influence on the meridional flow than differential rotation. We consider the LCT flow profiles from MDI as the ground truth. The comparison of LCT and *Optical Flow* methods with the MDI results is shown in Figure 7. The *Optical Flow* method can produce slightly better differ-



**62** Page 12 of 16 Q. Li et al.

ential rotation profiles than the LCT method at low latitudes and can even reach higher latitudes than 60°. LCT starts to produce overestimated flow at a lower latitude compared to *Optical Flow*, where the local flows surpass the rotation rate. For meridional flows, *Optical Flow* deduces a more consistent flow result within 45°, with a difference of 2.1 m s<sup>-1</sup>, and keep the decreasing trend until 65°, with a difference of 10.6 m s<sup>-1</sup>. The flow deduced from LCT has a mean difference of 15.6 m s<sup>-1</sup>, yet does not show a similar meridional flow-like trend. For pattern tracking methods, high-latitude flows are strongly affected by LOS projections effects, which can also be exaggerated by a highly dynamic environment such as the chromosphere. Therefore, the high-latitude flows of the chromosphere are characterized by sub-pixel motions and rapid feature evolution. Increasing the cadence cannot resolve this issue as the pattern is evolving faster.

# 4. Summary and Discussion

In order to provide transverse flows at the solar surface for an extended period of time, different datasets are needed for the task, especially  $H\alpha$  images, which cover 100 years of solar observations. To line up the  $H\alpha$  flow maps with photospheric flow maps, we generated global-scale flow maps from HMI for the period June 2010 to August 2020 and MDI for the period January 2000 to December 2010 using LCT, and we introduced the new self-supervised optical flow tracking method to generate transverse flows using  $H\alpha$  images.

The average flow profiles derived from HMI and MDI proved the reliability of LCT on global-scale photospheric transverse velocities in tens of years. The derived differential rotation profiles are in good agreement with helioseismic measurements that indicate 2.85  $\mu rad\,s^{-1}$  at the equator, and the accuracy holds until 60° for the MDI and 75° for the HMI dataset, respectively. Meridional flow, on the other hand, shows a similar trend with the helioseismic measurements, with a maximum flow speed of 25 m s $^{-1}$  at 30° for the MDI, and 35 m s $^{-1}$  at 40° for the HMI dataset, respectively. A proper linear transformation needs to be implemented to compare the flows from different measurements using pattern-tracking methods.

The chromosphere exhibits ubiquitous structures, including supergranular cells and spicules. While spicules consist of small dark features that are ubiquitous, they are also transient and thus may be suppressed in the 2-min cadence and further minimized through averaging. Additionally, averaging over both the east and west sides will reduce the contribution of their upward motions. On the other hand, the supergranular structure, which spans over 30,000 km and 24 hours, is believed to be the primary source of measurement, while active regions, plages and regular filaments also contribute to the measurements. Our objective is to measure the movements of all large-size and long-lived structures while suppressing short-lived or sparsely distributed features through averaging. While testing both methods on HMI, they were comparable in velocity distribution. Optical Flow exhibited stronger velocity amplitude than LCT, which is expected as LCT underestimates the velocity magnitude. In measuring chromospheric flows, LCT results were impacted by the highly dynamic background, leading to blurred flow profile that cannot recognize the meridional flow. The difference between KSO LCT and MDI can reach up to 20 m s<sup>-1</sup> at low latitudes. Conversely, Optical Flow method generates the differential rotation and meridional flow profiles from H $\alpha$  datasets that can be compared with surface flows using other methods and datasets and can be used to provide consensus observational constraints.

When deriving transverse velocities using LCT and Optical Flow, the following error sources may affect the flow profiles: systematic errors and image quality errors. In image



**Table 2** Uncertainty measurements of differential rotation and meridional flow from HMI/MDI magnetograms and KSO H $\alpha$  observations using LCT and *Optical Flow* methods. Top and bottom panels represent the error estimates from 30-day and 1-year windows.

Latitude	Differential rotation (μrad s <sup>-1</sup> )			Meridional flow (m s <sup>-1</sup> )				
	HMI	MDI	KSO(OF)	KSO(LCT)	HMI	MDI	KSO(OF)	KSO(LCT)
0 - 10	±0.048	±0.053	$\pm 0.307$	$\pm 0.909$	±11.38	±15.82	$\pm 28.07$	±31.02
10 - 20	$\pm 0.053$	$\pm 0.081$	$\pm 0.307$	$\pm 0.909$	$\pm 10.37$	$\pm 13.97$	$\pm 26.66$	$\pm 22.89$
20 - 30	$\pm 0.049$	$\pm 0.116$	$\pm 0.310$	$\pm 0.939$	$\pm 5.77$	$\pm 18.22$	$\pm 26.86$	$\pm 32.22$
30 - 40	$\pm 0.083$	$\pm 0.176$	$\pm 0.320$	$\pm 1.021$	$\pm 5.37$	$\pm 22.87$	$\pm 31.54$	$\pm 38.96$
40 - 50	$\pm 0.102$	$\pm 0.298$	$\pm 0.354$	$\pm 1.517$	$\pm 5.13$	$\pm 39.49$	$\pm 31.91$	$\pm 61.20$
50 - 60	$\pm 0.147$	$\pm 0.540$	$\pm 0.440$	$\pm 2.177$	$\pm 6.55$	$\pm 66.15$	$\pm 30.05$	$\pm 56.07$
60 - 70	$\pm 0.204$	$\pm 0.815$	$\pm 0.603$	$\pm 3.068$	$\pm 5.13$	$\pm 50.07$	$\pm 27.71$	$\pm 69.14$
70 - 80	$\pm 0.845$	$\pm 1.777$	$\pm 0.678$	$\pm 7.209$	$\pm 12.47$	$\pm 2.67$	$\pm 21.53$	$\pm 48.22$
0 - 10	$\pm 0.036$	$\pm 0.048$	$\pm 0.274$	$\pm 0.807$	$\pm 7.69$	$\pm 14.01$	$\pm 22.47$	$\pm 29.98$
10 - 20	$\pm 0.040$	$\pm 0.088$	$\pm 0.276$	$\pm 0.766$	$\pm 7.07$	$\pm 14.83$	$\pm 22.21$	$\pm 27.43$
20 - 30	$\pm 0.051$	$\pm 0.103$	$\pm 0.287$	$\pm 0.981$	$\pm 6.69$	$\pm 15.28$	$\pm 22.93$	$\pm 29.53$
30 - 40	$\pm 0.065$	$\pm 0.146$	$\pm 0.301$	$\pm 1.177$	$\pm 5.21$	$\pm 20.99$	$\pm 28.36$	$\pm 37.32$
40 - 50	$\pm 0.077$	$\pm 0.208$	$\pm 0.337$	$\pm 1.439$	$\pm 4.33$	$\pm 28.47$	$\pm 29.53$	$\pm 41.67$
50 - 60	$\pm 0.106$	$\pm 0.277$	$\pm 0.419$	$\pm 1.932$	$\pm 5.14$	$\pm 43.80$	$\pm 29.12$	$\pm 46.09$
60 - 70	$\pm 0.149$	$\pm 0.412$	$\pm 0.591$	$\pm 2.709$	$\pm 4.87$	$\pm 48.22$	$\pm 29.37$	$\pm 58.49$
70-80	$\pm 0.916$	$\pm 1.407$	$\pm 0.649$	±5.428	$\pm 10.42$	±51.99	±26.81	±52.12

quality errors, spatial resolution, cadence, and elapsed time may affect the flow results. For each of the data sources, a few tests were carried out to find the proper parameters. After choosing a few sets of these parameters that are good enough to detect the continuous flow velocities, different values of these parameters will still change the flow result by around 15%. The local-scale flow requires the elapsed time to precisely cover the lifetime of the tracking pattern. Otherwise, the actual velocities will be easily underestimated. In the case of global-scale flows, we choose a longer elapsed time as the transverse velocity becomes stable after a few hours of tracking. Apart from center-to-limb variation, there were minor discrepancies in the disk enter position in MDI images. Both MDI and HMI images also exhibit small changes in  $B_0$  and  $P_0$  angles that could impact the speed of rotation and meridional flow (Hathaway, Upton, and Mahajan, 2022) in less than 10 m s<sup>-1</sup>. Regarding the systematic errors due to the choice of the velocity representation, we show the 30-day and 1year uncertainty measurements of differential rotation and meridional flow from HMI/MDI magnetograms and KSO H $\alpha$  observations in Table 2. The standard deviation of the flow speed is calculated over 30-day and 1-year period at each latitude. Note that the standard deviation of KSO flows is also calculated from the mean flows from MDI. Yearly averaged flows for all data types are improved compared with the 30-day averaged flows. The MDI LCT differential rotation profile yields to an average of 7.3% relative error from 0° to 60°. At 60°, the turning point, an overestimated angular speed is due to the limitation of spatial resolution. The HMI LCT differential rotation profile yields to an average of 3.5% relative error from  $0^{\circ}$  to  $70^{\circ}$ , and loses the accuracy after  $\sim 75^{\circ}$ , where the angular speed has been overestimated. The KSO LCT differential rotation profile exhibits an average of 11.6% relative error from 0° to 50° and the turning point occurs after that, while the KSO Optical Flow has an average of 16.1% relative error from 0° to 60°. The meridional flow profiles



**62** Page 14 of 16 Q. Li et al.

show an "error band". The extrema of the meridional flow are the manifestation of sensitive signal variation because of the projection effect. In particular, the  $B_0$ -angle exhibits an annual variation due to the orbit of Earth around the Sun, which has a strong impact on where the heliographic center is located and the projection of transverse flows. However, the meridional flow derived from KSO H $\alpha$  exhibits more than two to three times the inaccuracy level than that from magnetograms, which is affected by numerous mass flows on the chromosphere.

Acknowledgments This work is supported by NSF Earthcube grant AGS-1927578 and NASA grant 80NSSC20K0182. MV acknowledges support by grant VE 1112/1-1 of the German Research Foundation (DFG). CD and MV acknowledge support by the European Commission's Horizon 2020 Program under grant agreements 824064 (ESCAPE – European Science Cluster of Astronomy & Particle Physics ESFRI Research Infrastructures) and 824135 (SOLARNET – Integrating High Resolution Solar Physics). We thank the KSO, SDO/HMI, and SoHO/MDI teams for providing the data. SoHO is a project of international collaboration between ESA and NASA.

**Author contributions** Qin, Yan, and Haimin wrote the main manuscript text. Junwei provides the helioseismology result in Figure 4. Meetu and Carsten provide the codes of data preprocessing and LCT. All authors reviewed the manuscript.

#### **Declarations**

**Competing interests** The authors declare no competing interests.

Open Access This article is licensed under a Creative Commons Attribution 4.0 International License, which permits use, sharing, adaptation, distribution and reproduction in any medium or format, as long as you give appropriate credit to the original author(s) and the source, provide a link to the Creative Commons licence, and indicate if changes were made. The images or other third party material in this article are included in the article's Creative Commons licence, unless indicated otherwise in a credit line to the material. If material is not included in the article's Creative Commons licence and your intended use is not permitted by statutory regulation or exceeds the permitted use, you will need to obtain permission directly from the copyright holder. To view a copy of this licence, visit http://creativecommons.org/licenses/by/4.0/.

## References

- Asensio Ramos, A., Requerey, I.S., Vitas, N.: 2017, DeepVel: deep learning for the estimation of horizontal velocities at the solar surface. Astron. Astrophys. 604, A11. DOI. ADS.
- Basu, S., Antia, H.M., Tripathy, S.C.: 1999, Ring diagram analysis of near-surface flows in the Sun. Astrophys. J. 512(1), 458. DOI. ADS.
- Beck, J.G.: 2000, A comparison of differential rotation measurements (invited review). *Solar Phys.* **191**(1), 47. DOI. ADS.
- Brajša, R., Wöhl, H., Vršnak, B., Ruždjak, V., Clette, F., Hochedez, J.-F.: 2001, Solar differential rotation determined by tracing coronal bright points in SOHO-EIT images. I. Interactive and automatic methods of data reduction. Astron. Astrophys. 374, 309. DOI. ADS.
- Braun, D.C.: 2019, Flows around averaged solar active regions. Astrophys. J. 873(1), 94. DOI. ADS.
- Chae, J., Sakurai, T.: 2008, A test of three optical flow techniques—LCT, DAVE, and NAVE. *Astrophys. J.* **689**(1), 593. DOI. ADS.
- Chandra, S., Vats, H.O., Iyer, K.N.: 2009, Differential coronal rotation using radio images at 17 GHz. Mon. Not. Roy. Astron. Soc. 400(1), L34. DOI. ADS.
- Chatterjee, S., Hegde, M., Banerjee, D., Ravindra, B., McIntosh, S.W.: 2020, Time-latitude distribution of prominences for 10 solar cycles: a study using Kodaikanal, Meudon, and Kanzelhohe data. *Earth Space Sci.* 7(3), e00666. DOI. ADS.
- Dikpati, M., Gilman, P.A., Ulrich, R.K.: 2010, Physical origin of differences among various measures of solar meridional circulation. *Astrophys. J.* **722**(1), 774. DOI. ADS.
- Domingo, V., Fleck, B., Poland, A.I.: 1995, The SOHO mission: an overview. *Solar Phys.* **162**(1 2), 1. DOI. ADS.



- Dosovitskiy, A., Fischer, P., Ilg, E., Hausser, P., Hazirbas, C., Golkov, V., Van Der Smagt, P., Cremers, D., Brox, T.: 2015, Flownet: learning optical flow with convolutional networks. In: *Proceedings of the IEEE International Conference on Computer Vision*, 2758.
- Fisk, L.A., Zhao, L.: 2009, The heliospheric magnetic field and the solar wind during the solar cycle. In: Gopalswamy, N., Webb, D.F. (eds.) *Universal Heliophysical Processes* **257**, 109. DOI. ADS.
- Gizon, L., Cameron, R.H., Pourabdian, M., Liang, Z.-C., Fournier, D., Birch, A.C., Hanson, C.S.: 2020, Meridional flow in the Sun's convection zone is a single cell in each hemisphere. *Science* 368(6498), 1469. DOI. ADS.
- Hao, Q., Fang, C., Cao, W., Chen, P.F.: 2015, Statistical analysis of filament features based on the Hα solar images from 1988 to 2013 by computer automated detection method. Astrophys. J. Suppl. 221(2), 33. DOI. ADS.
- Hathaway, D.H., Rightmire, L.: 2010, Variations in the Sun's meridional flow over a solar cycle. Science 327(5971), 1350. DOI. ADS.
- Hathaway, D.H., Upton, L.: 2014a, The solar meridional circulation and sunspot cycle variability. *J. Geophys. Res. Space Phys.* 119(5), 3316. DOI. ADS.
- Hathaway, D.H., Upton, L.: 2014b, The Sun's meridional flow and its role in magnetic flux transport and the sunspot cycle. In: AGU Fall Meeting Abstracts 2014, SH44A. ADS.
- Hathaway, D.H., Upton, L.A., Mahajan, S.S.: 2022, Variations in differential rotation and meridional flow within the Sun's surface shear layer 1996–2022. *Front. Astron. Space Sci.* **9**, 419. DOI. ADS.
- Hathaway, D.H., Gilman, P.A., Jones, H.P., Kasher, J., Simon, G.W. (GONG Nearly Steady Flows Team, GONG Magnetic Fields Team): 1996, GONG observations of solar surface flows. In: American Astronomical Society Meeting Abstracts 188, 53.04. ADS.
- Howard, R., Gilman, P.A.: 1986, Meridional motions of sunspots and sunspot groups. Astrophys. J. 307, 389.
  DOI. ADS.
- Howard, R., Labonte, B.J.: 1980, The Sun is observed to be a torsional oscillator with a period of 11 years. *Astrophys. J. Lett.* **239**, L33. DOI. ADS.
- Howe, R.: 2009, Solar interior rotation and its variation. Living Rev. Solar Phys. 6(1), 1. DOI. ADS.
- Howe, R., Hill, F., Komm, R., Chaplin, W.J., Elsworth, Y., Davies, G.R., Schou, J., Thompson, M.J.: 2018, Signatures of solar cycle 25 in subsurface zonal flows. Astrophys. J. Lett. 862(1), L5. DOI. ADS.
- Hur, J., Roth, S.: 2020, Optical flow estimation in the deep learning age. arXiv e-prints. arXiv.
- Hurlburt, N., Jaffey, S.: 2015, A spectral optical flow method for determining velocities from digital imagery. *Earth Sci. Inform.* **4**, 959. DOI. ADS.
- Imada, S., Fujiyama, M.: 2018, Effect of magnetic field strength on solar differential rotation and meridional circulation. Astrophys. J. Lett. 864(1), L5. DOI. ADS.
- Jørgensen, C.S., Karoff, C., Senthamizh Pavai, V., Arlt, R.: 2019, Christian Horrebow's sunspot observations I. Life and published writings. Solar Phys. 294(6), 77. DOI. ADS.
- Komm, R.W., Howard, R.F., Harvey, J.W.: 1993, Meridional flow of small photospheric magnetic features. Solar Phys. 147(2), 207. DOI. ADS.
- Komm, R., Howe, R., Hill, F.: 2018, Subsurface zonal and meridional flow during cycles 23 and 24. Solar Phys. 293(10), 145. DOI. ADS.
- Li, K.-J.: 2009, What does the Sun tell and hint now? Res. Astron. Astrophys. 9(9), 959. DOI. ADS.
- Liu, Y., Zhao, X., Hoeksema, J.T.: 2004, Correction of offset in MDI/SOHO magnetograms. Solar Phys. 219(1), 39. DOI. ADS.
- Liu, P., King, I., Lyu, M.R., Xu, J.: 2019, Ddflow: learning optical flow with unlabeled data distillation. In: *AAAI*. DOI.
- Longcope, D.W.: 2004, Inferring a photospheric velocity field from a sequence of vector magnetograms: the minimum energy fit. Astrophys. J. 612(2), 1181. DOI. ADS.
- Löptien, B., Birch, A.C., Duvall, T.L., Gizon, L., Schou, J.: 2016, The shrinking Sun: a systematic error in local correlation tracking of solar granulation. *Astrophys.* 590, A130. DOI. ADS.
- Löptien, B., Birch, A.C., Duvall, T.L., Gizon, L., Proxauf, B., Schou, J.: 2017, Measuring solar active region inflows with local correlation tracking of granulation. Astron. Astrophys. 606, A28. DOI. ADS.
- Mahajan, S.S., Hathaway, D.H., Muñoz-Jaramillo, A., Martens, P.C.: 2021, Improved measurements of the Sun's meridional flow and torsional oscillation from correlation tracking on MDI and HMI magnetograms. Astrophys. J. 917(2), 100. DOI. ADS.
- Mayer, N., Ilg, E., Häusser, P., Fischer, P., Cremers, D., Dosovitskiy, A., Brox, T.: 2015, A large dataset to train convolutional networks for disparity, optical flow, and scene flow estimation. arXiv e-prints. arXiv.
- November, L.J., Simon, G.W.: 1988, Precise proper-motion measurement of solar granulation. *Astrophys. J.* 333, 427. DOI. ADS.
- Parker, E.N.: 1955, Hydromagnetic dynamo models. Astrophys. J. 122, 293. DOI. ADS.
- Pesnell, W.D., Thompson, B.J., Chamberlin, P.C.: 2012, The Solar Dynamics Observatory (SDO). Solar Phys. 275, 3. DOI. ADS.



**62** Page 16 of 16 Q. Li et al.

Pötzi, W., Veronig, A.M., Temmer, M., Baumgartner, D.J., Freislich, H., Strutzmann, H.: 2016, 70 years of sunspot observations at the Kanzelhöhe observatory: systematic study of parameters affecting the derivation of the relative sunspot number. Solar Phys. 291(9-10), 3103. DOI. ADS.

- Rieutord, M., Roudier, T., Ludwig, H.-G., Nordlund, Å., Stein, R.: 2001, Are granules good tracers of solar surface velocity fields? Astron. Astrophys. 377, L14. DOI. ADS.
- Roudier, T., Švanda, M., Ballot, J., Malherbe, J.M., Rieutord, M.: 2018, Large-scale photospheric motions determined from granule tracking and helioseismology from SDO/HMI data. Astron. Astrophys. 611, A92. DOI. ADS.
- Scherrer, P.H., Bogart, R.S., Bush, R.I., Hoeksema, J.T., Kosovichev, A.G., Schou, J., Rosenberg, W., Springer, L., Tarbell, T.D., Title, A., Wolfson, C.J., Zayer, I. (MDI Engineering Team): 1995, The solar oscillations investigation Michelson Doppler Imager. Solar Phys. 162(1-2), 129. DOI. ADS.
- Scherrer, P.H., Schou, J., Bush, R.I., Kosovichev, A.G., Bogart, R.S., Hoeksema, J.T., Liu, Y., Duvall, T.L., Zhao, J., Title, A.M., Schrijver, C.J., Tarbell, T.D., Tomczyk, S.: 2012, The Helioseismic and Magnetic Imager (HMI) investigation for the Solar Dynamics Observatory (SDO). Solar Phys. 275(1-2), 207. DOI. ADS.
- Schroeter, E.H.: 1985, The solar differential rotation present status of observations. Solar Phys. 100, 141. DOI. ADS.
- Schuck, P.W.: 2005, Local correlation tracking and the magnetic induction equation. Astrophys. J. Lett. 632(1), L53. DOI. ADS.
- Sheeley, N.R. Jr.: 2005, Surface evolution of the Sun's magnetic field: a historical review of the flux-transport mechanism. Living Rev. Solar Phys. 2(1), 5. DOI. ADS.
- Shen, Z., Diercke, A., Denker, C.: 2018, Calibration of full-disk He I 10830 Å filtergrams of the Chromospheric Telescope. Astron. Nachr. 339(661), 661. DOI. ADS.
- Solanki, S.K., Usoskin, I.G., Kromer, B., Schüssler, M., Beer, J.: 2004, Unusual activity of the Sun during recent decades compared to the previous 11,000 years. *Nature* 431(7012), 1084. DOI. ADS.
- Steenbeck, M., Krause, F., Rädler, K.-H.: 1966, Berechnung der mittleren Lorentz-Feldstärke  $\overline{v \times \mathfrak{B}}$  für ein elektrisch leitendes Medium in turbulenter, durch Coriolis-Kräfte beeinflußter Bewegung. Z. Naturforsch. Teil A 21, 369. DOI. ADS.
- Thompson, W.T.: 2006, Coordinate systems for solar image data. Astron. Astrophys. 449(2), 791. DOI. ADS.
  Tlatova, K.A., Vasil'eva, V.V., Tlatov, A.G.: 2020, Drift of polar prominences in solar cycles 13–24. Geomagn. Aeron. 59(8), 1022. DOI. ADS.
- Ulrich, R.K.: 2010, Solar meridional circulation from Doppler shifts of the Fe I line at 5250 Å as measured by the 150-foot solar tower telescope at the Mt. Wilson Observatory. Astrophys. J. 725(1), 658. DOI. ADS
- Verma, M., Denker, C.: 2011, Horizontal flow fields observed in Hinode G-band images. I. Methods. Astron. Astrophys. 529, A153. DOI. ADS.
- Verma, M., Denker, C.: 2012, Horizontal flow fields observed in Hinode G-band images. III. The decay of a satellite sunspot and the role of magnetic flux removal in flaring. Astron. Astrophys. 545, A92. DOI. ADS.
- Verma, M., Steffen, M., Denker, C.: 2013, Evaluating local correlation tracking using CO<sup>5</sup>BOLD simulations of solar granulation. Astrophys. 555, A136. DOI. ADS.
- Wöhl, H., Brajša, R., Hanslmeier, A., Gissot, S.F.: 2010, A precise measurement of the solar differential rotation by tracing small bright coronal structures in SOHO-EIT images. Results and comparisons for the period 1998 – 2006. Astron. Astrophys. 520, A29. DOI. ADS.
- Xu, Y., Banerjee, D., Chatterjee, S., Pötzi, W., Wang, Z., Ruan, X., Jing, J., Wang, H.: 2021, Migration of solar polar crown filaments in the past 100 years. Astrophys. J. 909(1), 86. DOI. ADS.
- Zhao, J., Kosovichev, A.G.: 2004, Torsional oscillation, meridional flows, and vorticity inferred in the upper convection zone of the Sun by time-distance helioseismology. Astrophys. J. 603(2), 776. DOI. ADS.
- Zhao, J., Nagashima, K., Bogart, R.S., Kosovichev, A.G., Duvall, J.T.L.: 2012, Systematic center-to-limb variation in measured helioseismic travel times and its effect on inferences of solar interior meridional flows. *Astrophys. J. Lett.* 749(1), L5. DOI. ADS.
- Zhao, J., Bogart, R.S., Kosovichev, A.G., Duvall, J.T.L., Hartlep, T.: 2013, Detection of equatorward meridional flow and evidence of double-cell meridional circulation inside the Sun. Astrophys. J. Lett. 774(2), L29. DOI. ADS.

**Publisher's Note** Springer Nature remains neutral with regard to jurisdictional claims in published maps and institutional affiliations.

